ACS APPLIED MATERIALS & INTERFACES

www.acsami.org

Research Article

Exceptionally Uniform and Scalable Multilayer MoS_2 Phototransistor Array Based on Large-Scale MoS_2 Grown by RF Sputtering, Electron Beam Irradiation, and Sulfurization

Heekyeong Park,[⊥] Na Liu,[⊥] Bong Ho Kim,[⊥] Soon Hyeong Kwon, Seungho Baek, Sehwan Kim, Han-Koo Lee, Young Joon Yoon,* and Sunkook Kim*

Cite This: *ACS Appl. Mater. Interfaces* 2020, 12, 20645−20652

Read Online

ACCESS | Metrics & More | Article Recommendations | Supporting Information

ABSTRACT: Two-dimensional molybdenum disulfide (MoS_2) has emerged as a promising material for optoelectronic applications because of its superior electrical and optical properties. However, the difficulty in synthesizing large-scale MoS_2 films has been recognized as a bottleneck in uniform and reproducible device fabrication and performance. Here, we proposed a radio-frequency magnetron sputter system, and post-treatments of electron beam irradiation and sulfurization to obtain large-scale continuous and high-quality multilayer MoS_2 films. Large-area uniformity was confirmed by no deviation of electrical performance in fabricated MoS_2 thin-film transistors (TFTs) with an average on/off ratio of 10^3 and a transconductance of 0.67 nS. Especially, the photoresponsivity of our MoS_2 TFT reached 3.7 A W^{-1}, which is a dramatic improvement over that of a previously reported multilayer MoS_2 TFT (0.1 A W^{-1}) because of the photogating effect induced by the formation of trap states in the band gap. Finally, we organized a 4 × 4 MoS_2 phototransistor array with high photosensitivity, linearity, and uniformity for light detection, which demonstrates the great potential of 2D MoS_2 for future-oriented optoelectronic devices.

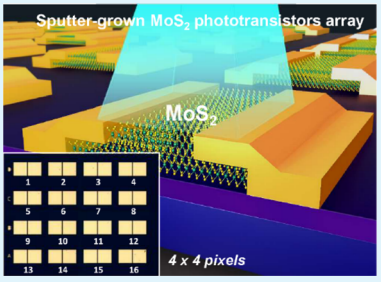

KEYWORDS: *MoS_2, phototransistor array, sputtering, electron beam irradiation, sulfurization*

1. INTRODUCTION

Two-dimensional transition metal dichalcogenides (TMDs) have gained considerable attention because of their ultrathin atomic-layered structures, excellent electrical and optical properties, and great potential applications for future nanoscale electronic and optoelectronic devices.[1−3] Among the TMDs, MoS_2 is the most extensively studied material because it has a semiconducting property with a layer-dependent band gap (1.2−1.8 eV) and a relatively high current on/off ratio (I_{on}/I_{off}) (~10^9) and carrier mobility (>10 cm^2 V^{-1} s^{-1}).[4−6] MoS_2 is also a promising channel material for photodetector applications.[7] Zhang et al. fabricated phototransistors based on a chemical vapor deposition (CVD)-grown monolayer MoS_2 with an excellent photoresponsivity and photogain of 2200 A W^{-1} and 5000, respectively.[8] Choi et al. presented multilayer MoS_2 phototransistors with a relatively high-photoresponsivity of 0.1 A W^{-1}.[9] Many attempts to improve the photoresponse of the MoS_2 photodetectors have been performed. These include surface sensitization,[10] surface plasmon resonance via nanoparticles,[11] surface treatment,[12] fabrication of nanoribbons,[13] and the stacking of hetero-structures.[14]

MoS_2 photodetectors can be used as a building block in optoelectronic systems such as image sensors and photologic gates. However, these applications are considerably limited by the difficulty of large-dimensional production of the MoS_2 atomic layer. Top-down approaches such as mechanical exfoliation and liquid-phase exfoliation typically produce MoS_2 flakes with few layers of relatively small size.[15−17] These exfoliation approaches exhibit no reproducibility and no layer controllability, making their application in large-scale advanced optoelectronics difficult. Therefore, many bottom-up growth methods such as CVD, physical vapor deposition (PVD), atomic layer deposition (ALD), and metalorganic chemical vapor deposition (MOCVD) are considered as solutions to realize large-scale photodetector arrays. ALD and MOCVD have already succeeded in growing MoS_2 atomic layers.[18,19] Despite the fact that the MoS_2 layer has high uniformity and high crystallinity, the growth rate is low and the cost is high. Recently, the growth of the centimeter-scale monolayer and few-layer MoS_2 were already synthesized using CVD.[20,21] However, in the thin-film industry, a sputtering technique is a facile technique and widespread commercialization to deposit uniform semiconducting films, such as amorphous silicon (α-Si), polycrystalline silicon (poly-Si),

Received: February 7, 2020
Accepted: April 13, 2020
Published: April 13, 2020

https://dx.doi.org/10.1021/acsami.0c02393
ACS Appl. Mater. Interfaces 2020, 12, 20645−20652

and indium gallium zinc oxide (IGZO). The large-area MoS_2 films deposited using sputtering have been previously reported.[22−24] The as-sputtered MoS_2 films were always post-annealed in a sulfur environment to increase their crystallinities. The size of a continuous few-layer MoS_2 directly sputtered on a silicon oxide (SiO_2) substrate was shown to reach a centimeter scale, and the MoS_2 field effect transistor showed good property through CVD sulfurization.[25] The MoS_2 layer number can be controlled by controlling the thickness of the sputtering film. The sputtering MoS_2 films combined with sulfurization exhibit large scale, good uniformity, and crystallinity, but their photoelectronic properties are very poor and even no phototransistor array has been realized. Electron beam irradiation (EBI) is used to induce atomic rearrangement through inelastic scattering, resulting in the crystallization of MoS_2.[26] However, the EBI-treated MoS_2 also shows extremely low photoresponsivity due to the insufficient crystallinity and sulfur vacancies.[27]

In this study, we present MoS_2 phototransistor arrays constructed on large-dimensional MoS_2 films grown using a radio-frequency (RF) magnetron sputtering deposition method combined with post-treatments processes. High-quality centimeter-scale trilayer MoS_2 was achieved by sputtering, EBI, and sulfurization. Microscopy and spectroscopy analyses confirmed that the post-treatments rearrange atoms in MoS_2 films, resulting in improvement of MoS_2 crystallinity. In addition, the MoS_2 films exhibit a 2H structure, which ensures good electrical performance of MoS_2 transistors. Fabricated MoS_2 phototransistors show a high photoresponsivity of 3.7 A W^{-1}. Moreover, the photoresponsive performance of the MoS_2 phototransistors is proven to be stable and uniform, which enables a 4 × 4 array to be produced. This work represents a new platform for future applications in the field of optoelectronics and image devices.

2. EXPERIMENTAL SECTION

2.1. MoS_2 Film Preparation. In our experiment, (100) oriented p-type (boron-doped with a resistivity <0.005 Ω m) Si/SiO_2 (300 nm) substrates were used. Prior to the synthesis of MoS_2 thin films, the substrates were ultrasonically cleaned by immersion in acetone, ethanol, and isopropyl alcohol solutions. Then, amorphous MoS_2 thin films were deposited on the substrate through RF magnetron sputtering at room temperature. A high-purity MoS_2 target (99%) with a 50.8 mm diameter was used for sputtering, and a base pressure of the sputtering chamber was maintained below 10^{-6} Torr. A working pressure was maintained at 5 mTorr with an Ar flow rate of 10 sccm, and an RF power of 20 W was applied. Prior to every sputtering process, the target was presputtered for 5 min to clean the surface of the target. The EBI process was conducted in the same chamber as that for sputtering. An electron gun with a 60 mm diameter extracted electrons from inductively coupled plasma. Then, the electron gun collimated and accelerated electrons to the amorphous as-deposited MoS_2 thin films. The inductively coupled plasma was generated with an RF power of 300 W, and the extracted electrons were accelerated by a DC energy of 3 kV for 1 min. A working pressure was maintained at 0.8 mTorr with an Ar flow rate of 10 sccm. The EBI-treated MoS_2 was inserted in the CVD chamber for sulfurization, which was conducted at 950 °C in a Ar (50 sccm)/H_2S (1 sccm, 10% H_2S)/H_2 (5 sccm) environment for 1 h.

2.2. Characterizations. Synthesized MoS_2 films were transferred onto Cu grids with a lacey carbon support film for plan-view transmission electron microscopy (TEM), and cross-sectional view samples were prepared by a single-beam focused ion beam system (FB-2100, Hitachi). Plan-view and cross-sectional TEM images were obtained by JEM-2100F (JEOL) and JEM-ARM200F (JEOL), respectively, with an accelerating voltage of 200 kV. Raman spectra were collected by (Alpha 300 S, WITec) using a 532 nm laser and 1800 grooves/mm grating. In addition, atomic force microscopy (AFM) (Alpha 300 S, WITec) was used to measure the thickness of the MoS_2 films. Chemical bonding states and stoichiometry of synthesized MoS_2 were investigated using an X-ray photoelectron spectroscopy (XPS) system (Nexsa, Thermo Scientific) with a pass energy of 50 eV. To apply the MoS_2 films for photoemission spectroscopy (PES) analysis, the MoS_2 films were transferred onto a conducting substrate using a conventional poly(methyl methacrylate) method. The secondary band edge and electron distribution near the valence band were measured by PES (4D-PES, Pohang light source-II) under ultrahigh vacuum (10^{-9} Torr). The measurement was conducted using synchrotron radiation with an incident photon energy of 90 eV. All spectra were calibrated with the reference of sputtered Au, which has a Fermi edge at a binding energy of 0 eV.

2.3. Fabrication of the MoS_2 Phototransistor Array. The synthesized MoS_2 film was patterned as channels of a transistor array by conventional photolithography. The unnecessary portions outside the channels were etched using O_2 plasma reactive ion etching with 30 sccm at 50 W for 1 min. The source and drain electrodes were prepatterned using LOR 3B and a photoresist followed by electron beam evaporation of Ti (20 nm)/Au (100 nm). The device was annealed at 200 °C for 2 h in a vacuum chamber to improve the electrical junction. This was accomplished by removing organic residues and ionic impurities between MoS_2 and electrodes.

2.4. Electrical and Optical Measurements. The electrical properties of MoS_2 phototransistors were evaluated using a semiconductor characteristic system (4200-SCS, Keithley) in a dark box measurement environment. A fiber-coupled laser source (MCLS1, Thorlabs) with a wavelength of 405 nm was used to radiate the light in a perpendicular direction to the channel of the MoS_2 phototransistors.

3. RESULT AND DISCUSSION

3.1. Synthesis of the Large-Area MoS_2 Film. The fabrication process is schematically shown in Figure 1a−c, and

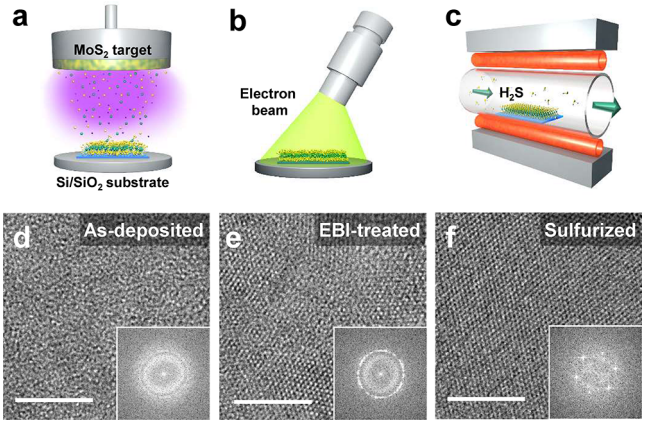

Figure 1. Synthesis process of the MoS_2 film and its atomic-scale structures. Schematic illustration of (a) sputtering, (b) EBI treatment, and (c) sulfurization. Plan-view TEM images and FFT patterns of (d) as-deposited, (e) EBI-treated, and (f) sulfurized MoS_2 films (all scale bars are 5 nm).

the detailed process is described in the Experimental Section. Amorphous MoS_2 films were deposited on Si/SiO_2 substrates by RF magnetron sputtering (Figure 1a), and the two post-processes of EBI treatment (Figure 1b) and sulfurization (Figure 1c) were subsequently conducted. For the EBI process, a low energy of 3 kV was applied for 1 min to induce inelastic scattering of electrons, resulting in atomic rearrangement by the interaction of incident electrons and electrons of the target

https://dx.doi.org/10.1021/acsami.0c02393
ACS Appl. Mater. Interfaces 2020, 12, 20645−20652

film.[26,28] Sulfurization was conducted at 950 °C in a H_2S and Ar environment for 1 h to enhance the crystallinity of the film.[25] The pictures of the MoS_2 films after sputtering, EBI treatment, and sulfurization showed purple, bluish purple, and blue, respectively (Figure S1a). The continuous blue exhibited in Figure S1b,c indicates that the sulfurized MoS_2 film is uniform in a large area.

3.2. Characteristics of Synthesized MoS_2 Films. The atomic-structural change of MoS_2 films, which was followed by post-treatments, was investigated by TEM analysis. Figure 1d–f shows plan-view TEM images and fast Fourier transform (FFT) patterns of the films. The amorphous structure of the as-deposited film was transformed into a polycrystalline structure after EBI treatment (Figure 1d,e), which was confirmed by the FFT pattern that transformed from a wide halo to a ring shape.[26] Several types of Moirè fringes in Figure 1e indicate that few layers of the MoS_2 film were stacked with rotation angles. After sulfurization, the crystallinity of the MoS_2 has a significant increase (Figure 1f). In addition, many grain boundaries were also observed in the MoS_2 film, indicating the polycrystalline (Figure S2).

To confirm the chemical bonding state and elemental composition of MoS_2 films, XPS was employed. Figure 2a shows high-resolution XPS spectra of Mo 3d and S 2p core levels of as-deposited, EBI-treated, and sulfurized MoS_2, including deconvolution curves. For the as-deposited MoS_2, the asymmetric peak at ~229.0 eV could be deconvoluted into two types of Mo ligands: Mo^{4+} $3d_{5/2}$ at ~229.4 eV corresponding to Mo–S bonding and Mo^0 $3d_{5/2}$ at ~228.5 eV corresponding to Mo–Mo bonding of Mo metal.[25] As previous studies have reported, 1 T-MoS_2 also exhibits a Mo 3d state at a similar binding energy as that of Mo^0.[29] However, no characteristic of the 1 T phase appears at a low binding energy of the S 2p signal. Thus, it can be inferred that the composition is Mo metal. In addition, a doublet appears at a high binding energy of the Mo 3d signal, which represents Mo^{6+} $3d_{5/2}$ ligands at 232.5 eV, corresponding to Mo–O bonding.[30] The Mo^{6+} 3d may derive from oxidation during the MoS_2 sputtering process, interfacial layer between MoS_2 and SiO_2, and the exposure of MoS_2 in the atmosphere.[25,31] The atomic fractions of the ligands in the Mo 3d and S 2p states are listed in Table 1. In the S 2p region, two groups of doublets are found. One of them is elemental S (S^0) where S $2p_{3/2}$ is located at a high binding energy of ~163.1 eV.[32] Moreover, S $2p_{3/2}$ at ~161.9 eV may be attributed to S^{2-} $2p_{3/2}$ ligands corresponding to S–Mo bonding.[30] The ratio of (S^0 + S^{2-}) 2p to Mo^{4+} 3d is approximately 3.38, which is greater than 2 and thus confirms the existence of elemental S. Therefore, as-deposited MoS_2 shows a low crystallinity that includes several species of impurities.

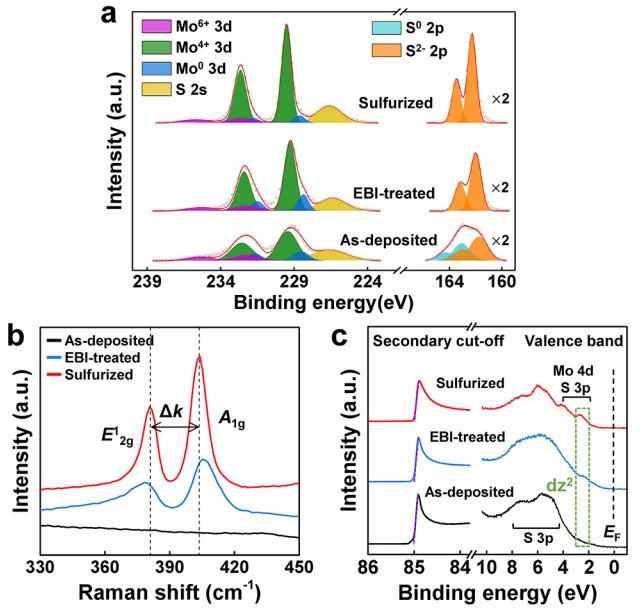

Figure 2. Spectroscopic analysis of MoS_2 films. (a) XPS spectra, (b) Raman spectra, and (c) secondary cutoff and valence band spectra obtained by PES analysis of as-deposited, EBI-treated, and sulfurized MoS_2 films, respectively.

Following EBI treatment, the atomic fraction of Mo^{6+} (Mo–O bonding) decreases and the peak of Mo^{4+} 3d ligand (Mo–S bonding) becomes sharp and strong. In addition to the fact that the terminal S^{2-} 2p ligand becomes dominant, elemental S^0 vanishes. These indicate that, during the EBI treatment, the Mo^{6+} oxide reacts with elemental S to form MoS_2. The atomic fraction of Mo^{4+} increases from 66.1 to 73.6% after EBI treatment. Moreover, the ratio of S^{2-} 2p to Mo^{4+} 3d is approximately 2.06, which is very close to the composition of MoS_2. The atomic fraction of Mo^0 experiences a slight decrease from 16.1 to 15.1% before and after EBI treatment. However, it dramatically reduces to 6.6% after sulfurization. This proves that Mo metal is simply sulfurized at a high temperature with gas H_2S to form MoS_2.[33] By contrast, the atomic fraction of Mo^{6+} undergoes practically no change after sequential post-treatments. It is inferred that the remaining Mo^{6+} oxide probably derives from the surface oxidation of MoS_2 during air exposure. In the sulfurized MoS_2, the atomic fraction of Mo^{4+} enhances to 82.4%, and the ratio of S^{2-} 2p to Mo^{4+} 3d is approximately 2.29, indicating a S-rich MoS_2. As shown in Figure 2a and Table 1, it was found that both Mo^{4+} 3d and S^{2-} 2p doublets in as-deposited MoS_2 have decreasing full-width at half-maximum (FWHM) and increasing intensity and area after EBI treatment and sulfurization. This demonstrates that, during the sequential post-treatments, a certain amount of MoS_2 is produced with enhanced crystallinity and homogeneity.

Raman spectra of the MoS_2 films are shown in Figure 2b. Two typical Raman peaks of in-plane (E^1_{2g}) and out-of-plane (A_{1g}) modes were not confirmed from the as-deposited film, whereas those peaks were prominently observed after EBI treatment and sulfurization, which well supports the atomic

Table 1. XPS Data of As-Deposited, EBI-Treated, and Sulfurized MoS_2

at% (FWHW)	Mo^{6+} $3d_{5/2}$ [232.5 ± 0.2 eV]	Mo^{4+} $3d_{5/2}$ [229.4 ± 0.1 eV]	Mo^0 $3d_{5/2}$ [228.5 ± 0.1 eV]	S^0 $2p_{3/2}$ [163.1 eV]	S^{2-} $2p_{3/2}$ [161.9 ± 0.2 eV]	(S^0 + S^{2-}) 2p :Mo^{4+} 3d
as-deposited	17.7%(2.2)	66.1%(1.6)	16.1%(1.2)	40.7%(1.5)	59.3%(1.6)	3.38:1
EBI-treated	11.3%(2.2)	73.6%(1.0)	15.1%(0.9)		100%(0.9)	2.06:1
sulfurized	11.0%(2.2)	82.4%(0.8)	6.6%(0.9)		100%(0.8)	2.29:1

https://dx.doi.org/10.1021/acsami.0c02393
ACS Appl. Mater. Interfaces 2020, 12, 20645–20652

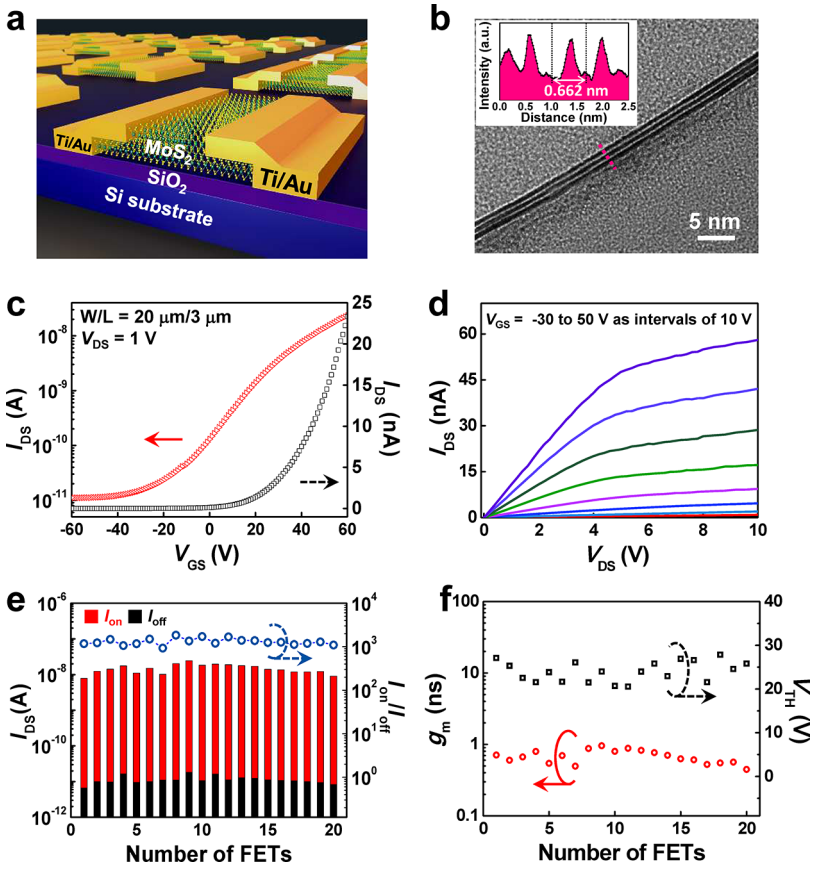

Figure 3. Electrical characteristics of MoS_2 TFTs. (a) Schematic image of MoS_2 TFTs, (b) cross-sectional TEM image of MoS_2 film and contrast intensity profile obtained from a marked line. (c) V_{GS}–I_{DS} curves at V_{DS} = 1 V, (d) V_{DS}–I_{DS} curves at V_{GS} from −30 to 50 V, (e) histogram of I_{on} and I_{off} and plot of I_{on}/I_{off}, and (f) plot of g_m and V_{TH} of 20 MoS_2 TFTs.

rearrangement.[34] More importantly, FWHM of two peaks of the EBI-treated film decreased from 15.7 to 7.8 cm^{-1} (E^1_{2g}) and from 12.3 to 8.5 cm^{-1} (A_{1g}) after sulfurization. The remarkable decrease in the FWHM of the E^1_{2g} mode indicates high atomic ordering in the layered structure because the E^1_{2g} mode derives from the parallel vibrations of Mo and S atoms with respect to the substrate.[35] In addition, the peak difference (Δk) between the E^1_{2g} and A_{1g} modes decreased from 25.6 to 23.4 cm^{-1} before and after sulfurization, which indicates a decrease in the number of layers from five to three.[31] Through AFM, the film thicknesses of as-deposited, EBI-treated, and sulfurized MoS_2 were measured at ∼4.5, ∼3.5, and ∼2.2 nm, respectively (Figure S3). This decrease in thickness was thought to have resulted from the atomic rearrangement induced by post-processing. To probe the microscale crystallinity of the MoS_2 film, the Raman mapping image in an area of 60 μm × 60 μm was measured. Figure S4a,b shows the Raman mapping characteristics of E^1_{2g} and A_{1g} modes centered at 380 and 403 cm^{-1}, respectively. The uniform color intensity suggests that the highly crystalline MoS_2 film is continuous and uniform in a large area. Moreover, 100 points of Raman characteristics on a 2 cm × 2 cm MoS_2 film were also measured and constructed a spatial map depicting the Δk between the E^1_{2g} and A_{1g} modes (Figure S5). About 77% points show Δk between 23 and 24 cm^{-1}, indicating a homogeneous trilayer MoS_2 in a centimeter scale.

Electrical structures of the synthesized MoS_2 films were characterized using PES. PES spectra in the secondary cutoff and valence band regions obtained by as-deposited, EBI-treated, and sulfurized MoS_2 films are shown in Figure 2c. The work function (ϕ) was defined as $\phi = h\nu - W$ where $h\nu$ = 90 eV and W is the spectral width extracted from the intersection of the slope of the secondary cutoff spectra with the background.[36] The work functions of as-deposited, EBI-treated, and sulfurized MoS_2 were calculated to be 4.97, 4.98, and 4.99 eV, respectively. The values were higher than those of previously reported MoS_2 films (4.52–4.92 eV) because the presence of the Mo–O bonding that was confirmed in the Mo 3d spectra of Figure 2a disturbs the electron emission from the surface.[36−39] It was previously reported that the oxidation of the MoS_2 film modulates the work function of up to 1.2 eV.[36] The variations of the work function of as-deposited, EBI-treated, and sulfurized films were approximately 0.01 eV, which was negligible. However, a band-tail was observed from the spectra of the as-deposited film, which is attributed to the inhomogeneity of the film, as confirmed in XPS analysis of the as-deposited film shown in Figure 2a.[39]

The right side of Figure 2c shows the valence band structure of three films below the Fermi energy (E_F = 0 eV). A valence band maximum (VBM) was estimated from the intersection of the slope of first states from E_F and the background.[40] The extracted VBMs were ∼3.36, ∼1.03, and ∼1.65 eV, respectively (Figure S6). As the band gap of the few-layer MoS_2 is estimated to be 1.29–1.9 eV,[41] it could be expected that the EBI-treated and sulfurized MoS_2 films are n-type semiconductors. To develop an in-depth understanding of the electrical structure of the three films, we compared the band

https://dx.doi.org/10.1021/acsami.0c02393
ACS Appl. Mater. Interfaces 2020, 12, 20645−20652

states under the VBM. It was previously reported that the visible states under an energy of 4 eV are derived from Mo 4d and S 3p bands, whereas those from 4 to 8 eV are assigned to S 3p origin.[39,40,42] It is noteworthy that the electron occupancy in the upper states associated with the d orbital of Mo atoms determines the electrical structure of MoS_2 as insulating, metallic, or semiconducting.[42,43] Although no peak was confirmed under 4 eV in the spectra of the as-deposited film, the EBI-treated film showed a peak near 2.5 eV and it became clearer on the sulfurized film. This peak was attributed to a completely occupied nonbonding d_z^2 band characteristically observed from semiconducting 2H-MoS_2.[7,43,44] As a result, it can be understood that the MoS_2 film underwent a transition from an amorphous to a semiconductor in the electrical structure through EBI treatment and sulfurization.

3.3. Electrical Properties of MoS_2 Thin-Film Transistors. Using the post-treated MoS_2 films, we fabricated thin-film transistors (TFTs), as shown in the schematic image of Figure 3a. The channel areas of the TFTs were patterned using photolithography and an etching process, and Ti/Au electrodes were deposited onto the MoS_2 film. Figure 3b shows a cross-sectional TEM image of a trilayer MoS_2 channel with an interlayer spacing of 0.66 nm (see the inset of Figure 3b), which is in accord with the results of Raman spectra (Figure 2b) and the AFM height profile (Figure S3c).

Figure 3c shows V_{GS}–I_{DS} curves of the MoS_2 TFT with a channel width (W) of 20 μm and length (L) of 3 μm in logarithmic and linear scales measured under V_{GS} from −60 to 60 V at a V_{DS} of 1 V. It exhibited a typical n-type semiconductor behavior with $I_{on}/I_{off} > 10^3$. In addition, low hysteresis of the transfer curve of the MoS_2 TFT was exhibited, as shown in the green curve in Figure S7. Based on the large hysteresis of the MoS_2 TFT without EBI treatment (blue curve), it could be expected that EBI treatment reduced the interfacial dangling bond and defects between the MoS_2 and SiO_2 substrate. V_{DS}–I_{DS} curves of the TFT were also measured in a V_{GS} range from −30 to 50 V at intervals of 10 V (Figure 3d), thus presenting an excellent ohmic contact behavior at a low V_{DS} and saturation at a high V_{DS}. These properties were unequivocally distinguished from the nonsemiconducting properties of as-deposited and EBI-treated MoS_2 TFT of the same W/L, as shown in Figure S8. The electrical current of as-deposited and EBI-treated MoS_2 TFTs was not controlled by gate voltage because of their valence band edge structure, as shown in Figure S6a,b. Although the VBMs of the two films were more than 1 eV different from E_F, the valence band-tails were very close to E_F (0 eV), which led to a barrier-less hole carrier flow.[45]

Statistics on the electrical characteristics of large-area grown MoS_2 TFTs were obtained by measuring 20 randomly distributed MoS_2 TFTs on a substrate (Figure S9). Figure 3e depicts on current (I_{on}) (red) and off current (I_{off}) (black) as well as the calculated I_{on}/I_{off} of each MoS_2 TFT. These present an average I_{on}/I_{off} of 1.3×10^3 with a standard deviation of ~17%. Both maximum transconductance (g_m) and the threshold voltage (V_{TH}) of MoS_2 TFTs were maintained within a certain range with an average of 0.67 nS and 24 V, respectively (Figure 3f). This superior electrical uniformity as well as the high yields of the MoS_2 TFTs obtained by sputtering, EBI treatment, and sulfurization were confirmed from these quantitative results, thus offering a critical advantage for designing large-area phototransistor matrices.

3.4. Photoresponsive Behavior of MoS_2 Phototransistors. As a first step toward producing a MoS_2 phototransistor array, we examined the photoresponsive characteristics of the MoS_2 TFT under illumination of various incident power densities (P_{inc}) from 1 to 220 mW cm^{-2} at an excitation wavelength (λ_{ex}) of 405 nm, as shown in Figure 4a. Measured

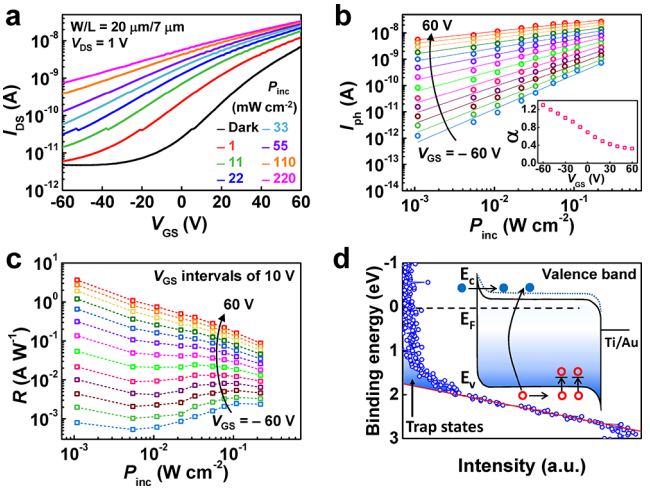

Figure 4. Photoresponsive behavior of MoS_2 TFT. (a) V_{GS}–I_{DS} curves of the MoS_2 phototransistor according to irradiation with λ_{ex} of 405 nm and various P_{inc}. (b) P_{inc}–I_{ph} at various V_{GS} range from −60 to 60 V as intervals of 10 V. (c) P_{inc}–R extracted from panel (b). (d) Density of state near VBM and schematic band diagram describing the mechanism of the PG effect on MoS_2 TFT.

V_{GS}–I_{DS} curves showed significant increases with an increase in P_{inc} over a full range of V_{GS} as compared to the dark state. To investigate a photocurrent (I_{ph}) generation mechanism of the MoS_2 phototransistor, we extrapolated V_{TH} of each curve and plotted the V_{TH} shift (ΔV_{TH}) as a function of P_{inc} in Figure S10a, which shows a very sharp decrease for a low P_{inc} and saturation for a high P_{inc}. Figure S10b shows V_{GS}–I_{DS} curves excluding the V_{TH} variation of each curve where the current still increased, especially in the off region.

The I_{ph} generation mechanisms of 2D material phototransistors are mainly modeled on the photogating (PG) and photoconductive (PC) effect.[46−48] The PG effect is derived from the local accumulation of carriers due to the existence of trap sites inside the channel.[47] This produces an additional effective gate voltage. The V_{TH} shift represents substantive evidence of the PG effect and gradually diminishes as the traps become saturated. By contrast, the PC effect represents a conductivity increase from the generation of excess carriers by an absorption of light, which is generally noticeable in the depletion regime.[9] Therefore, based on Figure S10a,b, we can expect the coexistence of both PG and PC effects on the performance of the MoS_2 phototransistor.

To confirm which of the two effects is dominant for our MoS_2 phototransistor, the relationship between the photocurrent and incident power density ($I_{ph} \propto P_{inc}^{\alpha}$) was considered, in which different absorption coefficients (α) were introduced from the PG ($\alpha < 1$) and PC ($\alpha \approx 1$) effects.[49,50] Figure 4b depicts I_{ph} ($I_{illumination} - I_{dark}$) as a function of P_{inc} for different V_{GS} ranging from −60 to 60 V at intervals of 10 V. Each α extracted from a slope of linearly fitted curves of $\log(I_{ph})$–$\log(P_{inc})$ was plotted (see the inset of Figure 4b) according to V_{GS}. It is noteworthy that α was close

https://dx.doi.org/10.1021/acsami.0c02393
ACS Appl. Mater. Interfaces 2020, 12, 20645−20652

to 1 in a negative V_{GS} region (off region) and became smaller ($\alpha < 1$) in a positive V_{GS} region (on region), indicating the dominant mechanism for generating a photocurrent changed from the PC to the PG effect as V_{GS} increased. Figure 4c shows the photoresponsivity ($R = I_{ph}/P_{inc}$) calculated from the data of Figure 4b. In the off region, the photoresponsivities were very low, whereas they reached as much as 3.7 A W^{-1} at 10^{-3} W cm^{-2} of P_{inc} at a V_{GS} of 60 V. Compared to the photoresponsivities of various phototransistors using multilayer MoS_2, as shown in Figure S11, it was found that the photoresponsivity of our MoS_2 phototransistor is in a high range. This high photoresponsivity of our MoS_2 phototransistor is thought to be achieved because of the PG effect that contributed to photocurrent generation over on state.

To determine the origin of the PG effect on our MoS_2 phototransistor, we focused on observing the inherent band gap structure that influences the carrier behavior. Figure 4d shows the density of state above the VBM (red line) at the Γ point in the Brillouin zone up to E_F (0 eV) obtained by PES measurement.[44] We produced direct evidence of photoassisted trap states, which are marked with blue areas in the band gap. A broad distribution of trap states extending to 1 eV below E_F was the result of imperfection and structural defects in MoS_2,[51] in here, the grain boundary and the existence of Mo−O bonding and Mo metal, which are confirmed in the XPS analysis, as shown in Figure 2a. We assumed that the interfacial defects between SiO_2 and MoS_2 were excluded here because of the effect of the EBI treatment (Figure S7). These abundant trap states capture the excess holes generated by light absorption, resulting in the accumulation of positive charges and an additional positive gate voltage. Thus, the effective Schottky barrier height is reduced and it increases the electron injection from the source, as shown in the schematic band diagram given as the inset of Figure 4d.

3.5. MoS_2 Phototransistor Array. We validated the capability of the MoS_2 for industrial applications in optoelectronics by achieving a uniformity of a large-dimensional synthesis and by overcoming the low photoresponsivity of a multilayer MoS_2. Based on these results, we fabricated a phototransistor array containing 4 × 4 MoS_2 phototransistors, as depicted on the left side of Figure 5a. Each phototransistor has a MoS_2 channel patterned with a W/L of 20 μm/5 μm and a Ti/Au electrode for source and drain contact (top right side of Figure 5a). A statistical distribution of the photoelectrical properties of 4 × 4 MoS_2 phototransistors was confirmed in the mapping images that present the current level of each phototransistor under the dark state and illumination with P_{inc} of 55 and 220 mW cm^{-2} (Figure 5b), respectively, where all current was measured at a V_{GS} of 60 V. As fully described in the previous section, MoS_2 phototransistors exhibited perfect uniformity with an average current value of 9.6 ± 2 nA under the dark state. When the light was on (bottom right side of Figure 5a), the current values of the elements averaged 20.7 (55 mW cm^{-2}) and 35.9 nA (220 mW cm^{-2}) with a very small standard deviation of 10 and 12%, respectively. This excellent consistency was confirmed by statistical results of photoresponsivity (R) and photosensitivity (S) of the matrix phototransistors as a function of P_{inc}, as depicted in Figure 5c,d. A small standard error and linear distribution of two characterizing factors are well worth the attention because they ensure ultrahigh uniformity in the phototransistor performance of the large-area MoS_2. The average photosensitivity of MoS_2 photodetectors could reach as high as 1.4 × 10^4 % at 0.2 W

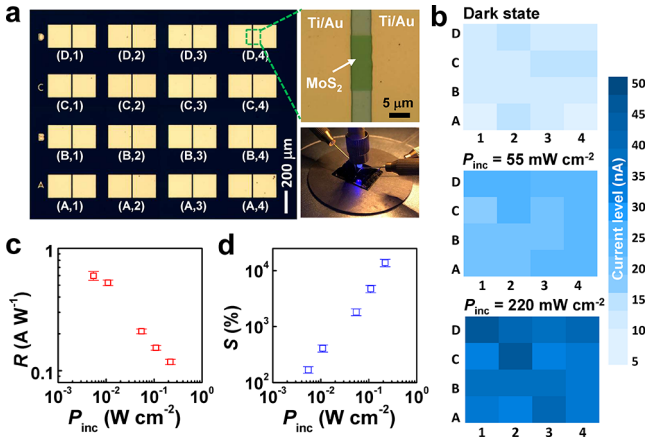

Figure 5. Phototransistor array consisting of 16 pixels of MoS_2 TFTs. (a) Optical image of the array (left), one pixel of MoS_2 phototransistor (upper right), and a picture of illumination on the device (bottom right). (b) Matrix images mapped to current variation under different P_{inc}. Average and standard error of (c) R and (d) S of 16 MoS_2 phototransistors according to P_{inc}, respectively.

cm^{-2} of P_{inc} (Figure 5d), thus indicating the suitability of our MoS_2 device for optoelectronic communication devices requiring ultrahigh photoelectrical performance. In addition, to confirm the reliability and reproducibility of the MoS_2 phototransistors, we measured the photoresponsivity of the 48 MoS_2 phototransistors (W/L of 20 μm/5 μm) on three different substrates under an illumination of P_{inc} of 11 mW cm^{-2}, as shown in Figure S12a−c. Figure S12d shows a distribution of photoresponsivity of 48 MoS_2 phototransistors with an average value of 0.503 A W^{-1} and only 15% of standard deviation, indicating a fully high stability and reproducibility of our MoS_2 phototransistor array.

4. CONCLUSIONS

We presented a phototransistor array based on a large-scale MoS_2 film synthesized by RF sputtering through post-processes of EBI treatment and sulfurization. The atomic rearrangement of MoS_2 films during the EBI treatment and sulfurization resulted in the transition of structural, chemical, and electrical characteristics to a 2H stacking semiconductor with an n-type property. The fabricated MoS_2 TFTs showed high uniformity in electrical properties such as I_{on}/I_{off}, g_m, and V_{TH}. We also confirmed the high photoresponsivity and photosensitivity of MoS_2 phototransistors, which were attributed to the predominant photogeneration mechanism of the PG effect induced by the formation of trap states near the valance band due to the structural imperfection and defects of MoS_2. Based on these superior performances, the 4 × 4 phototransistors array achieved highly sensitive, uniform, and reliable photodetection. These results provide a blueprint for the practical development of sputter-grown MoS_2 phototransistors and suggest further research directions for system-level integration with read-out circuits for future optoelectronic devices.

■ ASSOCIATED CONTENT

Supporting Information

The Supporting Information is available free of charge at https://pubs.acs.org/doi/10.1021/acsami.0c02393.

https://dx.doi.org/10.1021/acsami.0c02393
ACS Appl. Mater. Interfaces 2020, 12, 20645−20652

Optical images, AFM morphologies, and VBM extraction from PES spectra of as-deposited, EBI-treated, and sulfurized MoS_2 films; TEM images and Raman mapping images of the sulfurized MoS_2 film; $V_{GS}-I_{DS}$ of as-deposited and EBI-treated MoS_2 TFTs, $V_{DS}-I_{DS}$ of EBI-treated MoS_2 TFTs, and calculated g_m and I_{on}/I_{off} of 20 different EBI-treated MoS_2 TFTs; and the electrical characteristics of 20 MoS_2 TFTs and the photoresponsive characteristics of 48 MoS_2 phototransistors (PDF)

AUTHOR INFORMATION

Corresponding Authors

Young Joon Yoon − *Nanomaterials and Nanotechnology Center, Korea Institute of Ceramic Engineering and Technology, Jinju-si, Gyeongsangnam-do 52851, Republic of Korea*; Email: yjyoon@kicet.re.kr

Sunkook Kim − *School of Advanced Materials Science and Engineering, Sungkyunkwan University, Suwon-si, Gyeonggi-do 16419, Republic of Korea*; orcid.org/0000-0003-1747-4539; Email: seonkuk@skku.edu

Authors

Heekyeong Park − *School of Advanced Materials Science and Engineering, Sungkyunkwan University, Suwon-si, Gyeonggi-do 16419, Republic of Korea*

Na Liu − *School of Advanced Materials Science and Engineering, Sungkyunkwan University, Suwon-si, Gyeonggi-do 16419, Republic of Korea*

Bong Ho Kim − *Nanomaterials and Nanotechnology Center, Korea Institute of Ceramic Engineering and Technology, Jinju-si, Gyeongsangnam-do 52851, Republic of Korea*

Soon Hyeong Kwon − *Nanomaterials and Nanotechnology Center, Korea Institute of Ceramic Engineering and Technology, Jinju-si, Gyeongsangnam-do 52851, Republic of Korea*

Seungho Baek − *School of Advanced Materials Science and Engineering, Sungkyunkwan University, Suwon-si, Gyeonggi-do 16419, Republic of Korea*

Sehwan Kim − *School of Advanced Materials Science and Engineering, Sungkyunkwan University, Suwon-si, Gyeonggi-do 16419, Republic of Korea*

Han-Koo Lee − *Pohang Accelerator Laboratory, Pohang-si, Gyeongsangbuk-do 37673, Republic of Korea*

Complete contact information is available at: https://pubs.acs.org/10.1021/acsami.0c02393

Author Contributions

[⊥]H.P., N.L., and B.H.K. equally contributed to this work.

Notes

The authors declare no competing financial interest.

ACKNOWLEDGMENTS

This research was supported by the Basic Science Research Program of the National Research Foundation of Korea (NRF) funded by the Ministry of Science and ICT (2018R1A2B2003558, 2015R1A5A1037548, 2017R1D1A1B03032923, 2017R1D1A1B03035315). This research was partly supported by Gyeonggi-do Regional Research Center program of Gyeonggi province (GRRC Sungkyunkwan 2017-B06, Nano-biosensor based on flexible material).

REFERENCES

(1) Novoselov, K. S.; Jiang, D.; Schedin, F.; Booth, T. J.; Khotkevich, V. V.; Morozov, S. V.; Geim, A. K. Two-Dimensional Atomic Crystals. *Proc. Natl. Acad. Sci. U. S. A.* **2005**, *102*, 10451−10453.

(2) Schwierz, F. Nanoelectronics: Flat Transistors Get off the Ground. *Nat. Nanotechnol.* **2011**, *6*, 135−136.

(3) Wang, Q. H.; Kalantar-Zadeh, K.; Kis, A.; Coleman, J. N.; Strano, M. S. Electronics and Optoelectronics of Two-Dimensional Transition Metal Dichalcogenides. *Nat. Nanotechnol.* **2012**, *7*, 699−712.

(4) Mak, K. F.; Lee, C.; Hone, J.; Shan, J.; Heinz, T. F. Atomically Thin MoS_2: A New Direct-Gap Semiconductor. *Phys. Rev. Lett.* **2010**, *105*, 136805.

(5) Yoon, Y.; Ganapathi, K.; Salahuddin, S. How Good Can Monolayer MoS_2 Transistors Be? *Nano Lett.* **2011**, *11*, 3768−3773.

(6) Kim, S.; Konar, A.; Hwang, W. S.; Lee, J. H.; Lee, J.; Yang, J.; Jung, C.; Kim, H.; Yoo, J. B.; Choi, J. Y.; Jin, Y. W.; Lee, S. Y.; Jena, D.; Choi, W.; Kim, K. High-Mobility and Low-Power Thin-Film Transistors Based on Multilayer MoS_2 Crystals. *Nat. Commun.* **2012**, *3*, 1−7.

(7) Long, M.; Wang, P.; Fang, H.; Hu, W. Progress, Challenges, and Opportunities for 2D Material Based Photodetectors. *Adv. Funct. Mater.* **2019**, *29*, 1803807.

(8) Zhang, W.; Huang, J.-K.; Chen, C.-H.; Chang, Y.-H.; Cheng, Y.-J.; Li, L.-J. High-Gain Phototransistors Based on a CVD MoS_2 Monolayer. *Adv. Mater.* **2013**, *25*, 3456−3461.

(9) Choi, W.; Cho, M. Y.; Konar, A.; Lee, J. H.; Cha, G. B.; Hong, S. C.; Kim, S.; Kim, J.; Jena, D.; Joo, J.; Kim, S. High-Detectivity Multilayer MoS_2 Phototransistors with Spectral Response from Ultraviolet to Infrared. *Adv. Mater.* **2012**, *24*, 5832−5836.

(10) Kufer, D.; Lasanta, T.; Bernechea, M.; Koppens, F. H. L.; Konstantatos, G. Interface Engineering in Hybrid Quantum Dot-2D Phototransistors. *ACS Photonics* **2016**, *3*, 1324−1330.

(11) Miao, J.; Hu, W.; Jing, Y.; Luo, W.; Liao, L.; Pan, A.; Wu, S.; Cheng, J.; Chen, X.; Lu, W. Surface Plasmon-Enhanced Photodetection in Few Layer MoS_2 Phototransistors with Au Nanostructure Arrays. *Small* **2015**, *11*, 2392−2398.

(12) Jadwiszczak, J.; Li, G.; Cullen, C. P.; Wang, J. J.; Maguire, P.; Duesberg, G. S.; Lunney, J. G.; Zhang, H. Photoresponsivity Enhancement in Monolayer MoS_2 by Rapid O_2:Ar Plasma Treatment. *Appl. Phys. Lett.* **2019**, *114*, No. 091103.

(13) Li, Y.; Moy, E. C.; Murthy, A. A.; Hao, S.; Cain, J. D.; Hanson, E. D.; DiStefano, J. G.; Chae, W. H.; Li, Q.; Wolverton, C.; Chen, X.; Dravid, V. P. Large-Scale Fabrication of MoS_2 Ribbons and Their Light-Induced Electronic/Thermal Properties: Dichotomies in the Structural and Defect Engineering. *Adv. Funct. Mater.* **2018**, *28*, 1704863.

(14) Chen, C.; Feng, Z.; Feng, Y.; Yue, Y.; Qin, C.; Zhang, D.; Feng, W. Large-Scale Synthesis of a Uniform Film of Bilayer MoS_2 on Graphene for 2D Heterostructure Phototransistors. *ACS Appl. Mater. Interfaces* **2016**, *8*, 19004−19011.

(15) Lee, C.; Yan, H.; Brus, L. E.; Heinz, T. F.; Hone, J.; Ryu, S. Anomalous Lattice Vibrations of Single- and Few-Layer MoS_2. *ACS Nano* **2010**, *4*, 2695−2700.

(16) Coleman, J. N.; Lotya, M.; O'Neill, A.; Bergin, S. D.; King, P. J.; Khan, U.; Young, K.; Gaucher, A.; De, S.; Smith, R. J.; Shvets, I. V.; Arora, S. K.; Stanton, G.; Kim, H. Y.; Lee, K.; Kim, G. T.; Duesberg, G. S.; Hallam, T.; Boland, J. J.; Wang, J. J.; Donegan, J. F.; Grunlan, J. C.; Moriarty, G.; Shmeliov, A.; Nicholls, R. J.; Perkins, J. M.; Grieveson, E. M.; Theuwissen, K.; McComb, D. W.; Nellist, P. D.; Nicolosi, V. Two-Dimensional Nanosheets Produced by Liquid Exfoliation of Layered Materials. *Science* **2011**, *331*, 568−571.

(17) Zeng, Z.; Yin, Z.; Huang, X.; Li, H.; He, Q.; Lu, G.; Boey, F.; Zhang, H. Single-Layer Semiconducting Nanosheets: High-Yield Preparation and Device Fabrication. *Angew. Chem. Int. Ed.* **2011**, *50*, 11093−11097.

(18) Pyeon, J. J.; Kim, S. H.; Jeong, D. S.; Baek, S. H.; Kang, C. Y.; Kim, J. S.; Kim, S. K. Wafer-Scale Growth of MoS_2 Thin Films by Atomic Layer Deposition. *Nanoscale* **2016**, *8*, 10792−10798.

(19) Kang, K.; Xie, S.; Huang, L.; Han, Y.; Huang, P. Y.; Mak, K. F.; Kim, C.-J.; Muller, D.; Park, J. High-Mobility Three-Atom-Thick Semiconducting Films with Wafer-Scale Homogeneity. *Nature* **2015**, *520*, 656−660.
(20) Tao, L.; Chen, K.; Chen, Z.; Chen, W.; Gui, X.; Chen, H.; Li, X.; Xu, J.-B. Centimeter-Scale CVD Growth of Highly Crystalline Single-Layer MoS_2 Film with Spatial Homogeneity and the Visualization of Grain Boundaries. *ACS Appl. Mater. Interfaces* **2017**, *9*, 12073−12081.
(21) Yu, Y.; Li, C.; Liu, Y.; Su, L.; Zhang, Y.; Cao, L. Controlled Scalable Synthesis of Uniform, High-Quality Monolayer and Few-layer MoS_2 Films. *Sci. Rep.* **2013**, *3*, 1866.
(22) Huang, J.-H.; Chen, H.-H.; Liu, P.-S.; Lu, L.-S.; Wu, C.-T.; Chou, C.-T.; Lee, Y.-J.; Li, L.-J.; Chang, W.-H.; Hou, T.-H. Large-Area Few-Layer MoS_2 Deposited by Sputtering. *Mater. Res. Express* **2016**, *3*, No. 065007.
(23) Samassekou, H.; Alkabsh, A.; Wasala, M.; Eaton, M.; Walber, A.; Walker, A.; Pitkänen, O.; Kordas, K.; Talapatra, S.; Jayasekera, T.; Mazumdar, D. Viable Route towards Large-Area 2D MoS_2 Using Magnetron Sputtering. *2D Mater.* **2017**, *4*, No. 021002.
(24) Matsuura, K.; Ohashi, T.; Muneta, I.; Ishihara, S.; Kakushima, K.; Tsutsui, K.; Ogura, A.; Wakabayashi, H. Low-Carrier-Density Sputtered MoS_2 Film by Vapor-Phase Sulfurization. *J. Electron. Mater.* **2018**, *47*, 3497.
(25) Hussain, S.; Singh, J.; Vikraman, D.; Singh, A. K.; Iqbal, M. Z.; Khan, M. F.; Kumar, P.; Choi, D. C.; Song, W.; An, K. S.; Eom, J.; Lee, W. G.; Jung, J. Large-Area, Continuous and High Electrical Performances of Bilayer to Few Layers MoS_2 Fabricated by RF Sputtering via Post-Deposition Annealing Method. *Sci. Rep.* **2016**, *6*, 30791.
(26) Kim, B. H.; Gu, H. H.; Yoon, Y. J. Atomic Rearrangement of a Sputtered MoS_2 Film from Amorphous to a 2D Layered Structure by Electron Beam Irradiation. *Sci. Rep.* **2017**, *7*, 3874.
(27) Gu, H. H.; Kim, B. H.; Yoon, Y. J. Photoresponsive Behavior of Electron-Beam Irradiated MoS_2 Films. *Appl. Phys. Lett.* **2018**, *113*, 183103.
(28) Frantz, J.; Tarus, J.; Nordlund, K.; Keinonen, J. Mechanism of Electron-Irradiation-Induced Recrystallization in Si. *Phys. Rev. B* **2001**, *64*, 125313.
(29) Eda, G.; Yamaguchi, H.; Voiry, D.; Fujita, T.; Chen, M.; Chhowalla, M. Photoluminescence from Chemically Exfoliated MoS_2. *Nano Lett.* **2011**, *11*, 5111−5116.
(30) Brown, N. M. D.; Cui, N.; McKinley, A. An XPS Study of the Surface Modification of Natural MoS_2 Following Treatment in an RF-Oxygen Plasma. *Appl. Surf. Sci.* **1998**, *134*, 11−21.
(31) Muratore, C.; Hu, J. J.; Wang, B.; Haque, M. A.; Bultman, J. E.; Jespersen, M. L.; Shamberger, P. J.; McConney, M. E.; Naguy, R. D.; Voevodin, A. A. Continuous Ultra-Thin MoS_2Films Grown by Low-Temperature Physical Vapor Deposition. *Appl. Phys. Lett.* **2014**, *104*, 261604.
(32) Zhang, W.; Zhou, T.; Zheng, J.; Hong, J.; Pan, Y.; Xu, R. Water-Soluble MoS_3 Nanoparticles for Photocatalytic H_2 Evolution. *ChemSusChem* **2015**, *8*, 1464−1471.
(33) Lee, Y.; Lee, J.; Bark, H.; Oh, I. K.; Ryu, G. H.; Lee, Z.; Kim, H.; Cho, J. H.; Ahn, J. H.; Lee, C. Synthesis of Wafer-Scale Uniform Molybdenum Disulfide Films with Control over the Layer Number Using a Gas Phase Sulfur Precursor. *Nanoscale* **2014**, *6*, 2821−2826.
(34) Li, H.; Zhang, Q.; Yap, C. C. R.; Tay, B. K.; Edwin, T. H. T.; Olivier, A.; Baillargeat, D. From Bulk to Monolayer MoS_2: Evolution of Raman Scattering. *Adv. Funct. Mater.* **2012**, *22*, 1385−1390.
(35) Bertrand, P. A. Surface-Phonon Dispersion ofMoS_2. *Phys. Rev. B* **1991**, *44*, 5745−5749.
(36) Lee, S. Y.; Kim, U. J.; Chung, J.; Nam, H.; Jeong, H. Y.; Han, G. H.; Kim, H.; Oh, H. M.; Lee, H.; Kim, H.; Roh, Y. G.; Kim, J.; Hwang, S. W.; Park, Y.; Lee, Y. H. Large Work Function Modulation of Monolayer MoS_2 by Ambient Gases. *ACS Nano* **2016**, *10*, 6100−6107.
(37) Yun, J. M.; Noh, Y. J.; Yeo, J. S.; Go, Y. J.; Na, S. I.; Jeong, H. G.; Kim, J.; Lee, S.; Kim, S. S.; Koo, H. Y.; Kim, T. W.; Kim, D. Y. Efficient Work-Function Engineering of Solution-Processed MoS_2 Thin-Films for Novel Hole and Electron Transport Layers Leading to High-Performance Polymer Solar Cells. *J. Mater. Chem. C* **2013**, *1*, 3777−3783.
(38) Lin, J.; Zhong, J.; Zhong, S.; Li, H.; Zhang, H.; Chen, W. Modulating Electronic Transport Properties of MoS_2 Field Effect Transistor by Surface Overlayers. *Appl. Phys. Lett.* **2013**, *103*, No. 063109.
(39) Kadowaki, R.; Sano, N.; Abukawa, T. PEEM and Micro-UPS Studies of Cleaved and Exfoliated Molybdenum Disulfide Surfaces. *e-J. Surf. Sci. Nanotech.* **2017**, *15*, 115−120.
(40) Sarma, S.; Ghosh, B.; Ray, S. C.; Wang, H. T.; Mahule, T. S.; Pong, W. F. Electronic Structure and Magnetic Behaviors of Exfoliated MoS_2 Nanosheets. *J. Phys. Condens. Matter.* **2019**, *31*, 135501.
(41) Ganatra, R.; Zhang, Q. Few-Layer MoS_2: A Promising Layered Semiconductor. *ACS Nano* **2014**, *8*, 4074−4099.
(42) Böker, T.; Severin, R.; Müller, A.; Janowitz, C.; Manzke, R.; Voß, D.; Krüger, P.; Mazur, A.; Pollmann, J. Band Structure of MoS_2, $MoSe_2$, and α-$MoTe_2$: Angle-Resolved Photoelectron Spectroscopy and Ab Initio Calculations. *Phys. Rev. B* **2001**, *64*, 235305.
(43) Geng, D.; Cheng, Y.; Zhang, G.; Sun, X. A. *Layered Materials for Energy Storage and Conversion*; Royal Society of Chemistry: London, 2019; pp 286.
(44) McMenamin, J. C.; Spicer, W. E. Photoemission Studies of Layered Transition-Metal Dichalcogenides: MoS_2. *Phys. Rev. B* **1977**, *16*, 5474−5487.
(45) Kim, M.; Park, S.; Jeong, J.; Shin, D.; Kim, J.; Ryu, S. H.; Kim, K. S.; Lee, H.; Yi, Y. Band-Tail Transport of CuSCN: Origin of Hole Extraction Enhancement in Organic Photovoltaics. *J. Phys. Chem. Lett.* **2016**, *7*, 2856−2861.
(46) Island, J. O.; Blanter, S. I.; Buscema, M.; van der Zant, H. S. J.; Castellanos-Gomez, A. Gate Controlled Photocurrent Generation Mechanisms in High-Gain In_2Se_3 Phototransistors. *Nano Lett.* **2015**, *15*, 7853−7858.
(47) Fang, H.; Hu, W. Photogating in Low Dimensional Photodetectors. *Adv. Sci.* **2017**, *4*, 1700323.
(48) Furchi, M. M.; Polyushkin, D. K.; Pospischil, A.; Mueller, T. Mechanisms of Photoconductivity in Atomically Thin MoS_2. *Nano Lett.* **2014**, *14*, 6165−6170.
(49) Takanashi, Y.; Takahata, K.; Muramoto, Y. Characteristics of InAlAs/InGaAs High-Electron-Mobility Transistors under Illumination with Modulated Light. *IEEE Trans. Electron Devices* **1999**, *46*, 2271−2277.
(50) Kang, H. S.; Choi, C. S.; Choi, W. Y.; Kim, D. H.; Seo, K. S. Characterization of Phototransistor Internal Gain in Metamorphic High-Electron-Mobility Transistors. *Appl. Phys. Lett.* **2004**, *84*, 3780−3782.
(51) Siao, M. D.; Shen, W. C.; Chen, R. S.; Chang, Z. W.; Shih, M. C.; Chiu, Y. P.; Cheng, C. M. Two-Dimensional Electronic Transport and Surface Electron Accumulation in MoS_2. *Nat. Commun.* **2018**, *9*, 1442.

https://dx.doi.org/10.1021/acsami.0c02393
ACS Appl. Mater. Interfaces 2020, 12, 20645−20652